BNL-211293-2019-JAAM

Computational modeling of curcumin-based fluorescent probe molecules

V. Satalkar, Q. Wu

To be published in "THEORETICAL CHEMISTRY ACCOUNTS"

January 2019

Center for Functional Nanomaterials

Brookhaven National Laboratory

U.S. Department of Energy

USDOE Office of Science (SC), Basic Energy Sciences (BES) (SC-22)

DISCLAIMER

Computational Modeling of Curcumin Based Fluorescent Probe Molecules

Vardhan Satalkar,[1, a)] Theo A. Rusmore,[1, a)] Elizabeth Phillips,[2] Xiaoliang Pan,[1] Enrico Benassi,[3, 4] Qin Wu,[5] Chongzhao Ran,[6, b)] and Yihan Shao[1, c)]

[1)] *Department of Chemistry and Biochemistry, University of Oklahoma, Norman, Oklahoma 73019, USA*

[2)] *Stephenson School of Biomedical Engineering, University of Oklahoma, Norman, Oklahoma 73019, USA*

[3)] *School of Science and Technology, Nazarbayev University, 53 Qabanbay Batyr Ave., Astana 010000, Kazakhstan*

[4)] *Novosibirsk State University, Pirogova str. 2, Novosibirsk 630090, Russia*

[5)] *Center for Functional Nanomaterials, Brookhaven National Laboratory, Upton, New York 11973, USA*

[6)] *Molecular Imaging Laboratory, Athinoula A. Martinos Center for Biomedical Imaging, Massachusetts General Hospital and Harvard Medical School, Boston, Massachusetts, 02129, USA*

(Dated: 5 January 2019)

Abstract. In recent years, a series of curcumin analogs were designed as fluorescent probes for detecting and imaging Aβ peptide aggregates and reactive oxygen species (ROS) in Alzheimer's disease (AD) brains. In order to gain a better understanding of the photophysical properties of these probe molecules, a systematical computational investigation was performed using the time-dependent density functional theory (TDDFT) calculations. Computed absorption and emission wavelengths well reproduced the spectral shifts among the curcumin analogs. In particular, for a recently proposed pair of probe molecules, CRANAD-**5** and CRANAD-**61**, for sensing ROS in preclinical studies of AD brains, their emission wavelength difference was found to arise from a delocalization of the lowest unoccupied molecular orbital of CRANAD-**61** from the curcuminoid backbone to the oxalate moiety. Overall, this study reaffirms the value of employing TDDFT calculations to assist the design of new curcumin-based fluorescence probes for AD research.

[a] These two authors contributed equally

[b] Author to whom correspondence should be addressed; Electronic mail: cran@nmr.mgh.harvard.edu

[c] Author to whom correspondence should be addressed; Electronic mail: yihan.shao@ou.edu

I. INTRODUCTION

Alzheimer's Disease (AD) is a progressive and fatal neurodegenerative disease. AD research is crucial because it affects a large portion of the senior population and because currently there are neither preventative measures nor effective treatments for the disease.[1,2] It has been known for many years that Aβ plaques are produced during different stages of AD. However, the exact role of Aβ plaques in the progression of AD had been a subject of dispute,[3,4] largely because their abundance found in postmortem histological studies correlate poorly with the severity of the disease. One plausible explanation is that Aβ plaques can be categorized into "silent" (mature) plaques and "active" newly formed ones. The latter is regarded to be more toxic and leads to cell deaths through inhibiting mitochondrial function, calcium hemostasis, and other neuronal cell functions.[5]

It has been suggested that Aβ aggregates should be studied in conjunction with oxidative stresses,[6–9] because a higher reactive oxygen species (ROS) level is expected in AD brains than healthy ones. ROS can be produced during the formation and growth of new "active" Aβ plaques, specifically through the Fenton reaction of Aβ with metal ions during Aβ crosslinking. When ROS is accumulated, it can prompt a buildup of inflammatory cytokines, which then attacts microglia to surround the plaques,[10] consequently more ROS is released.[11] Therefore, relatively high concentrations of ROS can be viewed as a signature feature of "active" Aβ plaques, and its measurement provides a convenient technique to differentiate these plaques from "silent" ones.[12]

To address the many challenges facing the AD research, many efforts have been devoted to the detection and imaging of Aβ aggregates and, more recently, ROS in the brain (see Ref. 13 for a review). Thioflavin[14] and other early probes emit visible light, which poorly penetrates the tissue and blood brain barrier. More recently, several near infrared fluorescence (NIRF) probes were designed to target Aβ fibrils, such as NIAD-**4**,[15] BODIPY derivatives,[16] MCAAD-**3**,[17] DANIRs molecules,[18] and a series of curcumin analogues (CRANAD-X).[12,19–25] We note that computational modeling were carried out previously on Thioflavin,[26] NIAD-**4**,[27] DANIRs,[28] and potential new NIRF probes.[29] These calculations provided valuable insight into the photophysical properties of these fluorophores and their binding to Aβ fibrils.

In this work, we will focus on a series of boron-containing curcumin analogues (see Fig. 1)

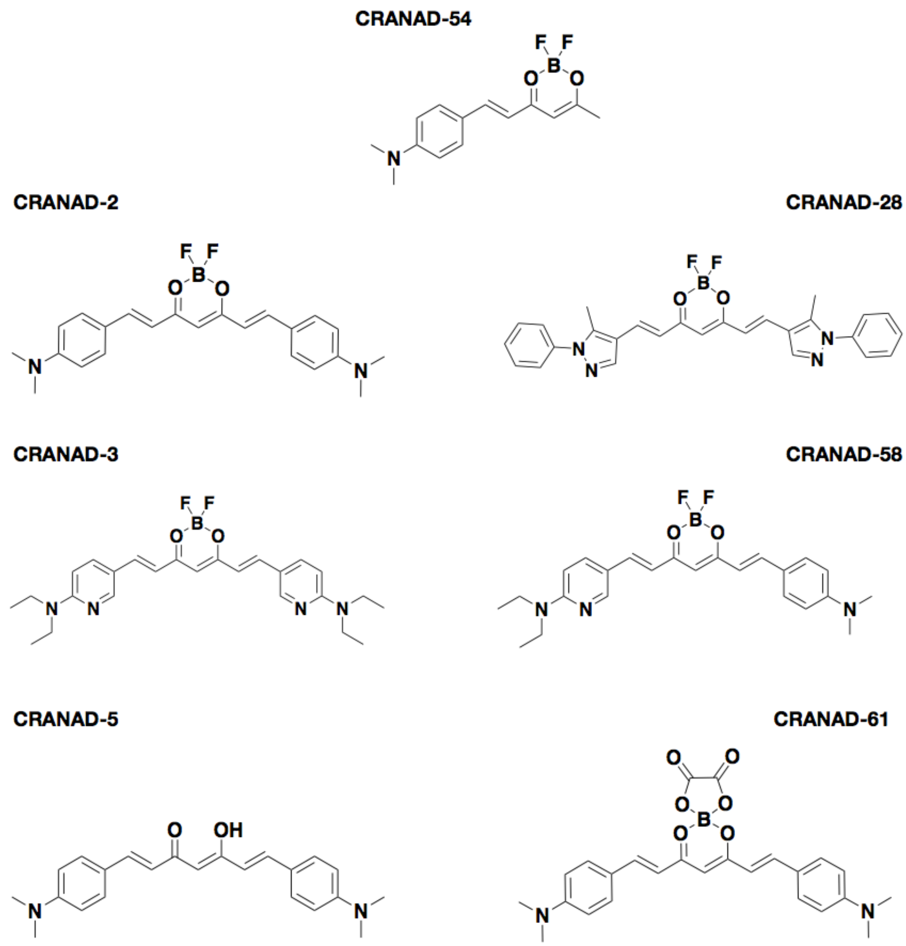

FIG. 1: CRANAD molecules

mentioned above,[12,19–22,30] which are called CRANAD molecules, for detecting Aβ aggregates and ROS. Among these molecules, CRANAD-**54** is the smallest. CRANAD-**2** combines a pull force from an electron accepting difluoroboryl (-BF_2) group and push forces from electron-donating dimethylamino groups at both ends of the curcumin molecule, which led to a red shifted emission relative to the curcumin molecule.[19] CRANAD-**2** molecule binds only to insoluble Aβ aggregates but not to soluble Aβs. To improve the binding, one (or both) of the hydrophobic phenyl moieties in CRANAD-2 can be replaced with a moderately hydrophilic pyridyl moiety. This leads to CRANAD-**3**[21] and CRANAD-**58**,[20] which displayed fluorescence responses to both soluble Aβ oligomers and insoluble aggregates. Another molecule, CRANAD-**28**,[31] was designed as a two-photon imaging probe.

Of particular interest are a pair of molecules, CRANAD-**5** and CRANAD-**61**,[12] which were developed recently as on-off NIRF probe molecules for sensing ROSs in AD brains. A standalone CRANAD-**61** fluorophore emits in the near-infrared (NIR) region. But it can readily react with hydrogen peroxide and other ROS in living cells and animals, leading to the removal of the oxalate moiety. The molecule is thus converted to CRANAD-**5**, whose emission blue-shifts to the visible region. So an injection of CRANAD-**61** into the brain and a subsequent time-course measurement of fluorescent emission intensities at two different wavelengths will yield information about the ROS concentration in the brain.[12]

In this article, a systematic computational modeling on CRANAD molecules will be reported. Specifically, we will investigate: (1) if the widely-used time-dependent density functional theory (TDDFT) calculations can be used to predict the spectral shifts among CRANAD molecule; (2) if the absorption/emission wavelengths of these molecules correlate well with the energy gap between the highest occupied molecular orbital (HOMO) and the lowest unoccupied molecular orbital (LUMO); and (3) what causes the difference in the emission wavelengths between CRANAD-**5** and CRANAD-**61** molecules?

We note that, very recently, Fages and coworkers performed a combined experimental and computational study of curcumoids with the borondifluoride moiety,[30] where they focused on the effect of introducing different functional groups at the terminal and meso positions of the curcumoid backbone. One of their analogs (**13** in Ref. 30), which contains a dimethylamino group at both terminals, was referred to as CRANAD-**2** earlier[19] and in this paper. In their work, Fages *et al.* compared observed emission energies, electrochemical gaps (based on oxidation/reduction potentials from cyclic voltametry measurements), and computed HOMO-LUMO gaps, and found a good correlation among these data. Compared to their work, we will study the electronic structure of four other borondifluoride-containing CRANAD molecules (**3**, **28**, **54**, and **58**). In addition, through studying a boron-oxalate-containing CRANAD molecule (**61**) and its unsubstituted counterpart (**5**), it will help us understand the effect of different boron-containing groups, such as $–BF_2$ and $–B(C_2O_4)$, on the ground state and excited state properties of curcuminoid fluorophores.

II. COMPUTATIONAL METHODS AND DETAILS

All quantum mechanical (QM) electronic ground-state calculations were performed using the density functional theory (DFT) method,[32,33] whereas excited-state calculations were carried out using the TDDFT method.[34,35] Version 5.0 of the Q-Chem software package[36] was used.

Functionals. Four density functionals, including B3LYP,[37–39] PBE0,[40] M06-2X,[41] and ωB97X-D,[42] were used for absorption energy calculations; while only B3LYP, PBE0, and ωB97X-D functionals were used in emission energy calculations (because TDDFT analytical nuclear gradient for meta functionals has yet to be implemented in the Q-Chem package). The performance of density functionals in TDDFT calculations has been well documented.[43–47] In general, hybrid functionals such as B3LYP and PBE0 are expected to perform well for localized (*i.e.* non-charge-transfer) valence excited states. Meanwhile, M06-2X and ωB97X-D functionals, with higher ratios of long-range Hartree-Fock exchange (54% and 100%, respectively), usually provide better descriptions for charge-transfer states.

Basis set and integration grid. Most of the results were obtained using a triple-zeta basis, 6-311++G**,[48] and SG-1 numerical integration grid,[49] which is a pruned Lebedev grid with 50 radial points and 194 angular points.[50] As shown in Table S1 in the electronic supplementary material, relative to 6-311++G** values, TDDFT absorption wavelengths (using the ωB97X-D funcitonal) for three representative molecules (CRANAD-**5**, **54**, and **61**) changed by no more than 1.3 nm with the 6-311+G(2d, p) basis, which was used in Ref. 30, and by no more than 8.2 nm with cc-pVTZ or aug-cc-pVTZ basis set. The effect of using larger integration grid is also small — the computed absorption wavelengths of three molecules in Table S2 changed by no more than 1.3 nm between SG-1 and the much more demanding (99, 590) grids.

Implicit solvent model. To account for the solvent effect, we employed the polarizable continuum model (PCM)[51] for water solvent molecules, specifically the C-PCM model[52,53] (as implemented in Q-Chem[36,54] using Bondi radii and a 1.2 scaling factor). For a comparison, some results using the integral equation formalism of PCM (IEF-PCM)[55] are shown in Tables S3 and S4, where the two solvent models led to differences of no more than 2.4 nm in the computed absorption wavelengths, and no more than 0.6 nm in the emission wavelengths. For absorption energy calculations, ground-state geometry optimization was performed using equilibrium PCM, then vertical excitation energies were computed using TDDFT and the non-equilibrium linear-response PCM model.[56,57] For a comparison, TDDFT absorption energies using a non-equilbrium perturbative state-specific model[58] are shown in Table S5, which differ by no more than 3.0 nm from values in Table I obtained using the linear-response model. For emission energy calculations, excited-state geometry optimization was performed using TDDFT energies using the equilibrium linear-response PCM model.

Validation with curcumin conformers. As an initial validation of our computational approach, we computed the ground-state energy (using the ωB97X-D functional) and absorption/emission energies of six conformers of the curcumin molecule. As shown in Fig. S1, the ground-state energy varied by up to 3.3 kcal/mol among these conformers, while the absorption energy changed by no more than 0.010 eV (ranging from 3.2805 to 3.2904 eV) and the emission energy by no more than 0.017 eV (ranging from 2.5716 to 2.5886 eV). Such small variation among planar curcumin conformers is consistent with the observation by Benassi *et al* based on B3LYP/6-31+G* and B3LYP/6-311+G** calculations.[59]

III. RESULTS AND DISCUSSIONS

A. From curcumin to CRANAD molecules

The natural curcumin molecule contains hydroxyl and methoxy groups at both terminals. In most CRANAD molecules shown in Fig. 1, the hydroxyl group is replaced with dimethylamino or diethylamino groups, while the methoxy group was removed from all molecules. The effect of such systematic structural substitutions on the electronic transition of curcumin molecule can be seen in Fig. S2.

Functional groups with different electron-donating strengths, as measured by their Hammett σ_p constants[60] [–H (0.0); –OH (-0.37); $–NH_2$ (–0.66); $-NMe_2$ (-0.83); $–NEt_2$ (-0.72)], were adopted in our calculations. For analogs without the methoxy groups (left column in Fig. S2), their computed absorption and emission energies clearly red shifted with stronger electron-donating groups at the para position. The same trend was observed with analogs with methoxy groups (right column in Fig. S2).

The effect of the methoxy group is more subtle. With small groups (–H, –OH, and $–NH_2$) at the para position, the addition of a methoxy group at the neighboring (meta) position led to a decrease of about 0.04 or 0.05 eV in the computed excitation energies. With more bulky groups, $–NMe_2$ and $–NEt_2$, the addition of a methoxy group led to a less planar structures and, therefore, to an increase of about 0.12–0.15 eV in the computed absorption energies. For the ground state of curcumin molecule containing adjacent methoxy and dimethylamino groups, both methyl groups were found to be out of the aryl plane with computed C–N–C–C dihedral angles of 14° and 64°. These angles are reduced to around 7°, in the absence of the methoxy group.

B. Keto-enol Tautomerization of CRANAD-5

In addition to the enol form, which was observed in X-ray structures,[61] the curcumin molecule can undergo keto-enol tautomerization.[24,25,62–65] Its diketo form comprises of a methylene group (–CH_2–), which is reactive in basic conditions due to the presence of two adjacent carbonyl groups. According to previous computational studies, the enol form was predicted to be about 7 kcal/mol lower than the diketo form,[64] with the latter adopting a non-planar structure. In agreement with these studies, our calculation indicated that the enol form is 2.40 – 5.63 kcal/mol lower in energy depending on the functional in use (Table S6). This indicated that the enol form of curcumin is predominant in the condensed phase. In addition, as shown in Table S6, the nonplanar diketo form is predicted to have a vertical excitation energy that is 0.5–0.7 eV higher than the enol form.

Among the seven CRANAD molecules in this study (Fig. 1), CRANAD-**5** is the only molecule that can also undergo keto-enol tautomerization. Our DFT calculations indicated, like the curcumin molecule, the enol form of CRANAD-**5** is also the energetically favorable conformer in the condensed phase. The keto-enol energy difference was predicted in Table S7 to be 0.92 kcal/mol at the ωB97X-D/6-311++G**/C-PCM level of theory, and 3.41 kcal/mol with the B3LYP functional. As shown in Fig. S3, the enol form of CRANAD-5 is nearly planar, with a O1–C1–C2–C3 dihedral angle of 0.3° and a C1–C2–C3–O2 angle of -0.3° within the ωB97X-D/6-311++G**/C-PCM level of theory. The diketo form of CRANAD-5 is non-planar (Fig. S4), where the O1-C1–C2–C3 angle is found to be 103.6° and the C1–C2–C3–O2 angle is -7.3°.

C. Absorption Wavelengths

Experimental absorption wavelengths for seven CRANAD molecules are listed in Table I. The shortest absorption wavelength was found for the shortest molecule: CRANAD-**54** (490 nm). The wavelength was slightly longer with CRANAD-**28** (498 nm) and CRANAD-**5** (530 nm). Much longer wavelengths were measured for other four molecules: CRANAD-**3**

(610 nm); CRANAD-**58** (630 nm); CRANAD-**2** (645 nm); and CRANAD-**61** (675 nm). All absorption energies were measured in the PBS buffer, which was approximated as water solvent in our computational study.

TABLE I: Absorption wavelengths (in nm) of CRANAD-X molecules from TDDFT/CPCM calculations using different functionals and 6-311++G** basis set.

Molecule	2	3	5	28	54	58	61
Expt.	645.0	610.0	530.0	498.0	490.0	630.0	675.0
B3LYP	593.1	573.7	534.2	470.4	473.6	585.0	610.0
PBE0	566.9	547.3	508.6	453.9	458.7	559.2	584.8
ωB97X-D	477.1	457.8	415.0	397.2	414.3	469.0	498.6
M06-2X	507.3	489.6	436.7	412.1	432.1	501.5	532.8

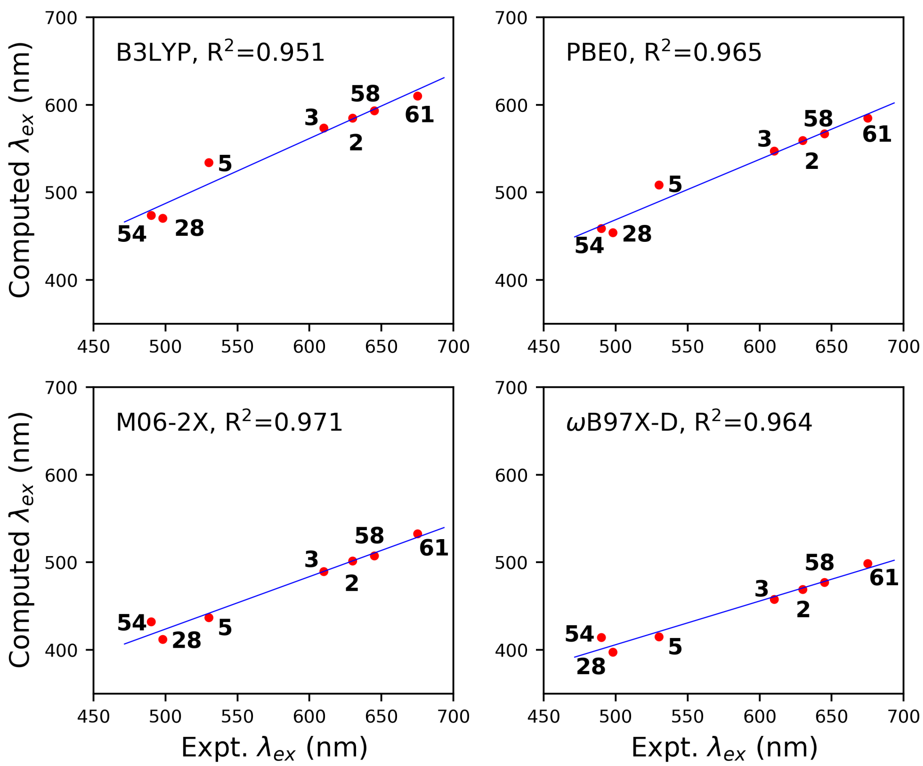

FIG. 2: Computed TDDFT absorption wavelengths (in nm) *vs* experimental values for CRANAD molecules.

Computed TDDFT absorption wavelengths using four different functionals (B3LYP, PBE0, M06-2X and ωB97X-D) were also listed in Table I. They are plotted against experimental values in Fig. 2. It is clear that TDDFT calculations reproduced the absorption spectral shifts rather well. Standard hybrid functionals, B3LYP and PBE0, yielded wavelengths closer to experimental values, and the corresponding R^2 values are 0.951 and 0.965, respectively. On the other hand, M06-2X and ωB97X-D functionals led to systematically shorter wavelengths, but with R^2 values of 0.971 and 0.964, a strong correlation was also observed between computed and experimental absorption wavelengths.

It is interesting to note that in Table I that, in almost all cases, TDDFT calculations consistently yielded shorter wavelengths than experimental values. The only exception was observed for CRANAD-**5**, where computed B3LYP absorption wavelength is longer by 4.2 nm than the experimental peak at 530 nm. This exception might arise from structural flexibilities of CRANAD-**5**. As the only CRANAD molecule in this study containing a β-keto enol group, CRANAD-**5** can undergo keto-enol tautomerization, intramolecular proton transfer, or hydroxyl deprotonation. It is therefore interesting to study the effect of these structural changes on its excitation energies.

Keto-enol tautomerization of CRANAD-**5** can lead to absorption at a shorter wavelength (for the diketo form). As mentioned in Section IIIB above, the (nonplanar) diketo form was found to be only 3.41 kcal/mol (or 0.92 kcal/mol) higher than the enol form based on B3LYP (or ωB97X-D) calculations. TDDFT calculations results in Table S7 showed that the absorption wavelengths of the diketo form were predicted to be 50–100 nm shorter than those of the enol form.

Intramolecular proton transfer can lead to a small red shift in the absorption wavelength. To study this effect, potential energy scan was performed with the proton moving between the two oxygen atoms (O1 and O2) in the enol form of CRANAD-**5**. As shown in Fig. S5, when the proton is moved from one oxygen atom towards the equidistance point, the ground-state energy was increased by about 2.5 kcal/mol. This is accompanied by a 0.05 eV reduction of the excitation energy, which amounts to a 7 nm increase in the absorption wavelength.

On the other hand, hydroxyl deprotonation can cause a blue-shift in the absorption wavelength. Upon the deprotonation of the hydroxyl group, CRANAD-**5** becomes an anion. As shown in the next subsection, the lowest-energy excitation involves the transfer of a small amount of electronic charge from the terminal groups towards the middle. This excitation will be hindered by more negative charges on the oxygen atom after hydroxyl deprotonation.

D. Wavefunction Analysis

In TDDFT calculations, the lowest-energy excitation of CRANAD molecules were found to be dominated by an excitation from HOMO to LUMO. So it would be worthwhile to examine the computed HOMO-LUMO gaps of these molecules. As is well known, the values of computed HOMO-LUMO gaps strongly depend on the functional in use, and, in general, their values increases with the ratio of the long-range Hartree-Fock exchange for the functional. This can be easily be seen in Fig. 3, where HOMO-LUMO gaps (y-axis values) follow the trend: B3LYP $<$ PBE0 $<$ M06-2X $<$ ωB97X-D. With each of these functionals, there is a strong correlation between HOMO-LUMO gaps and vertical excitation energies (x-axis values), with the correlation coefficients ranging from 0.938 (B3LYP) to 0.978 (M06-2X). This allows us to explain the variation of excitation energies of CRANAD molecules through studying the changes in their HOMOs and LUMOs.

Of particular interest to us is the red shift observed in the absorption wavelength from CRANAD-**5** to CRANAD-**61**. As shown in Fig. 4, the HOMO of CRANAD-**5** appeared very similar to that of CRANAD-**61**. These two Kohn-Sham orbitals have nearly the same energies, with values of -0.2548 a.u. (CRANAD-**5**) and -0.2564 a.u. (CRANAD-**61**) at the ωB97X-D/6-311++G** level of theory.

On the other hand, Fig. 4 shows a small but noticeable difference in the LUMOs of these two molecules. There is a small contribution from the oxalate moiety to the LUMO of CRANAD-**61**, which making the orbital slightly more delocalized than the LUMO of CRANAD-**5**. As a result, the LUMO energy of CRANAD-**61**, -0.0576 a.u., was substantially lower than the -0.0328 a.u. LUMO energy value for CRANAD-**5**. This led to a smaller HOMO-LUMO gap for CRANAD-**61** (0.1988 a.u.) than the gap of CRANAD-**5** (0.2220 a.u.), which in turn led to a relatively lower excitation energy (and longer absorption wavelength) for CRANAD-**61**.

The more delocalization nature of the electron excitation can also be seen in Fig. 5, which shows the unrelaxed difference densities (i.e. difference between the ground-state and excited-state electronic densities) of two molecules. For CRANAD-**61**, a small amount of electron density was transferred to the oxalate moiety upon the vertical excitation, and

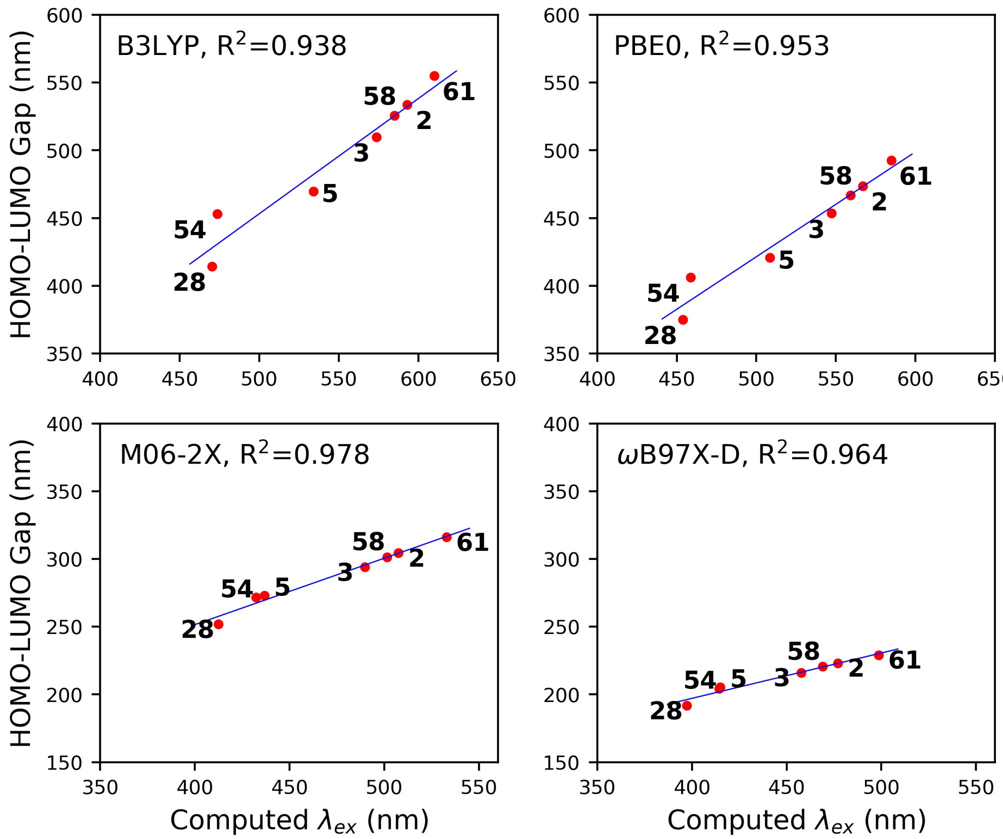

FIG. 3: HOMO-LUMO gaps *vs* TDDFT absorption excitation energies (in nm) of CRANAD-X molecules, all computed at ground-state equilibrium geometries.

the actual amount was found to be 0.0177 e$^-$ (Merz-Kollman ESP charge) and 0.0145 e$^-$ (Mulliken population) from TDDFT/ωB97X-D/6-311++G** calculations.

E. Emission Wavelengths

Experimental and computed emission wavelengths for CRANAD molecules are tabulated in Table II, and their values are also plotted in Fig. 6. Similar to the case of absorption calculations, TDDFT calculations with B3LYP and PBE0 functionals produced emission wavelengths closer to experimental values, while TDDFT calculations using the range-separated ωB97X-D functional tended to overestimate the excitation energies and thus underestimate the wavelengths. On the other hand, with all three functionals (B3LYP, PBE0, and ωB97X-D), TDDFT calculations well reproduced the experimentally observed spectral shift in the emission wavelengths among CRANAD molecules. The R^2 values were found to be 0.89–

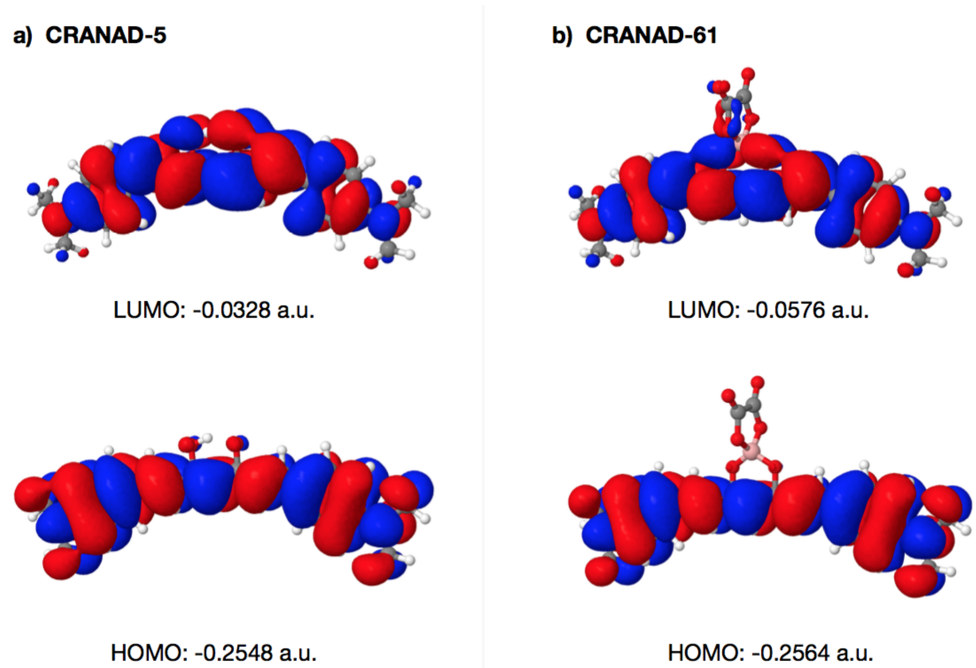

FIG. 4: HOMO and LUMO orbitals of CRANAD-**5** and CRANAD-**61** at the ωB97X-D/6-311++G** level of theory.

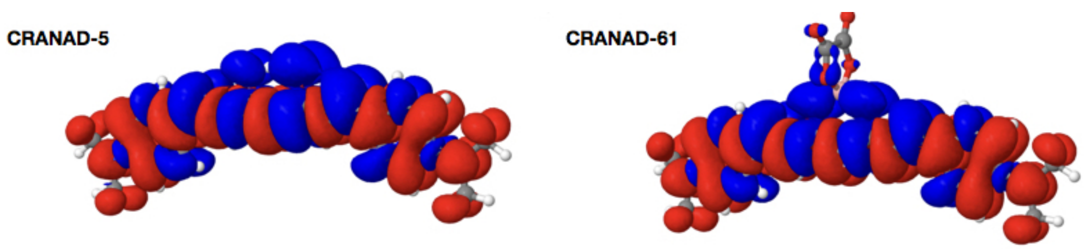

FIG. 5: Unrelaxed difference density of CRANAD-**5** and CRANAD-**61** from TDDFT/ωB97X-D/6-311++G** calculations. Blue color indicates a net gain of electron density, and red a net loss.

0.90 for all three (B3LYP, PBE0 and ωB97X-D) functionals. This reaffirms that TDDFT calculations with these functionals can be employed to predict emission spectral shifts of fluorescent probes such as CRANAD molecules.

F. Torsional energy profiles of CRANAD-54

Recently Segado, Benassi and Barone[59] studied the torsional energy profile of o-(p-dimethyl-amino-stryryl)methylpridinium cation (DASPMI). For this cationic molecule, tor-

TABLE II: Emission wavelengths (in nm) of CRANAD-X molecules from TDDFT/CPCM calculations using different functionals and 6-311++G** basis set.

Molecule	2	3	5	28	54	58	61
Expt.	805.0	730.0	669.0	578.0	620.0	750.0	760.0
B3LYP	696.7	664.7	620.3	564.4	551.0	685.8	720.8
PBE0	672.9	640.9	594.3	541.0	530.0	656.4	693.0
ωB97X-D	604.9	574.0	529.4	494.0	511.3	588.7	628.8

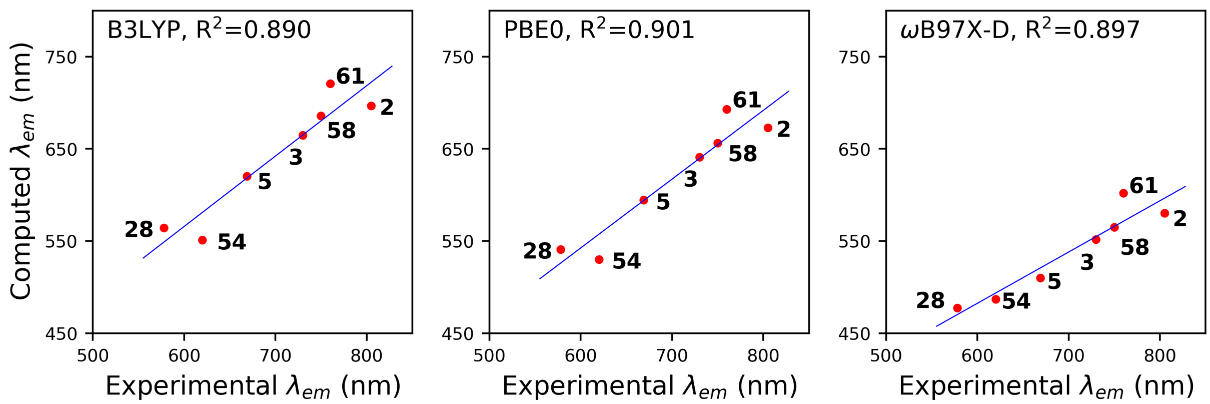

FIG. 6: Computed TDDFT emission wavelengths (in nm) *vs* experimental values for CRANAD-X molecules.

sional motions around three single bonds led to multiple minima on the excited-state potential energy surface, which causes nonemissive twisted intramolecular charge transfer (TICT) and multifluorescence.

To study whether TICT might affect CRANAD molecules, we followed their work and explored torsional energy profiles of CRANAD-**54**, which is the smallest molecule in our set of molecules. Fig. 7 clearly shows that, with each of the three torsional angles (T1, T2, and T3, see Fig. S11), both ground-state and excited state energies have a minimum around 180°. Therefore, TICT is unlikely to affect CRANAD-**54**. This also explains why geometry optimizations (for both absorption and emission calculations) led to nearly planar structures for the CRANAD molecules (see Tables S8 and S9).

Our torsional scan also showed the effect of boron-containing groups, such as $-BF_2$ and

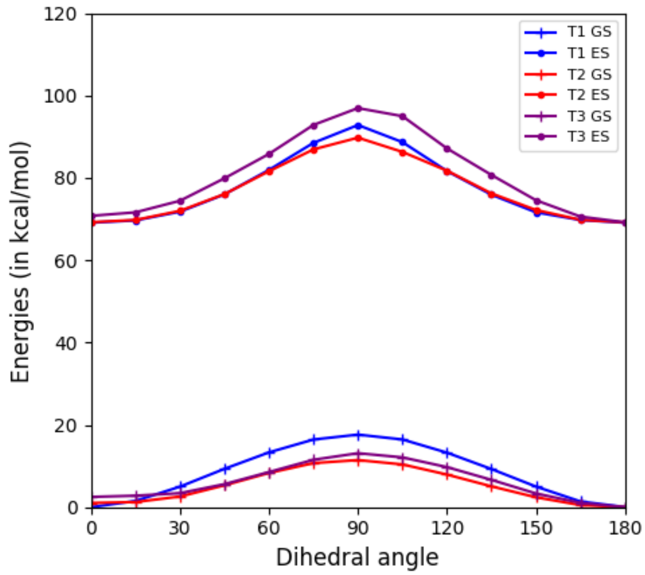

FIG. 7: Torsional energy profiles for CRANAD-**54** from three potential energy scans, with respect to T1, T2 and T3 angles. Ground state energies were optimized with ωB97X-D/6-311++G** with T1 or T2 or T3 constrained to a given value. Excited-state energy for each constrained geometry were computed using TDDFT and ωB97X-D/6-311++G**.

–$B(C_2O_4)$, on the rigidity of the half-curcumin scaffold in CRANAD-**54**. As shown in Fig. S11 and Table S11, in comparison to the keto-enol half-curcumin, both BF_2 and $B(C_2O_4)$ groups increased the ground-state barrier for all three rotations, which thus made these half-curcumin derivatives more rigid.

IV. CONCLUSIONS

Through performing TDDFT calculations of the lowest-energy electronic transition of CRANAD molecules, the following conclusions were reached:

- Computed TDDFT absorption and emission wavelengths well reproduced the spectral shifts among CRANAD molecules, with R^2 values of above 0.95 for absorption wavelengths and above 0.89 for emission wavelengths.

- Computed vertical excitation energies were found to correlate well with the HOMO-LUMO gaps. This supports the use of HOMO and LUMO energies in the analysis of the absorption/emission spectra shifts and in the design of new curcumin-based fluorescent molecules.

- Between the recently proposed pair of curcumin derivatives, CRANAD-**5** and CRANAD-**61**, the LUMO energy was lowered in CRANAD-**61** due to a contribution from the oxalate moiety, which extended the delocalization of the orbital.

At the same time, with a red-shift in the electronic transition energies and a related reduction in the HOMO-LUMO gaps, it becomes increasingly important to assess the multi-reference character of these systems. More sophisticated calculations, such as CASSCF, CASPT2, DMRG and RDM, will be performed in follow-up work.

ACKNOWLEDGMENTS

YS acknowledges financial support from Department of Energy grant No. DE-SC0011297 and from the University of Oklahoma startup fund. CR is supported by NIH grant No. R01AG055413. YS greatly appreciates insightful comments from Dr. Roland Lindh. Computational resources and services used in this work were provided by the OU Supercomputing Center for Education and Research (OSCER) and the Center of Functional Nanomaterials (CFN). CFN is a U.S. DOE Office of Science Facility, at the Brookhaven National Laboratory under Contract No. DE-SC0012704.

REFERENCES

[1] J. Hardy and D.J. Selkoe, "The Amyloid Hypothesis of Alzheimer's Disease:Progress and Problems on the Road to Therapeutics", *Science* **297**, 353—356 (2002).

[2] D.J. Selkoe, "Resolving Controversies on the Path to Alzheimer's Therapeutics", *Nat. Med.* **17**(9), 1060–1065 (2011).

[3] L.f. Lue, Y.m. Kuo, A.E. Roher, L. Brachova, Y. Shen, L. Sue, T. Beach, J.H. Kurth, R.E. Rydel, and J. Rogers, "Soluble Amyloid beta Peptide Concentration as a Predictor of Synaptic Change in Alzheimer's Disease", *Am. J. Pathol.* **155**, 853–862 (1999).

[4] C.A. Mclean, R.A. Cherny, F.W. Fraser, S.J. Fuller, M.J. Smith, K. Beyreuther, A.I. Bush, and C.L. Masters, "Soluble Pool of Abeta Amyloid as a Determinant of Severity of Neurodegeneration in Alzheimer's Disease", *Ann. Neurol.* **46**, 860–866 (1999).

[5]E. Giacobini and G. Gold, "Alzheimer Disease Therapy Moving from Amyloid beta to tau", *Nat. Rev. Neurol.* **9**, 677–686 (2013).

[6]D. Pratico, "Oxidative Stress Hypothesis in Alzheimer's Disease: a Reappraisal", *Trends Pharmacol. Sci.* **29**, 609–615 (2008).

[7]H. Xie, S. Hou, J. Jiang, M. Sekutowicz, J. Kelly, and B.J. Bacskai, "Rapid Cell Death is Preceded by Amyloid Plaque-Mediated Oxidative Stress", *Proc. Nat. Acad. Sci. USA* **110**, 7904–7909 (2013).

[8]X. Wang, W. Wang, L. Li, G. Perry, H.g. Lee, and X. Zhu, "Oxidative Stress and Mitochondrial Dysfunction in Alzheimer's Disease", *Biochim. Biophys. Acta* **1842**, 1240–1247 (2014).

[9]G.H. Kim, J.E. Kim, S.J. Rhie, and S. Yoon, "The Role of Oxidative Stress in Neurodegenerative Diseases", *Exp. Neurobiol.* **24**, 325–340 (2015).

[10]Y. Huang, N. Erdmann, H. Peng, Y. Zhao, and J. Zheng, "The role of TNF related apoptosis-inducing ligand in neurodegenerative diseases.", *Cell. Mol. Immunol.* **2**, 113–122 (2005).

[11]W.R. Markesbery, "Oxidative Stress Hypothesis in Alzheimer's Disease", *Free Radic. Biol. Med.* **23**, 134–147 (1997).

[12]J.J. Yang, X. Zhang, P. Yuan, J.J. Yang, Y. Xu, J. Grutzendler, Y. Shao, A. Moore, and C. Ran, "Oxalate-Curcumin Based Probe for Micro- and Macro-Imaging of Reactive Oxygen Species in Alzheimer's Disease.", *Proc. Nat. Acad. Sci. USA* **114**, 12384–12389 (2017).

[13]V. Patel, X. Zhang, N.A. Tautiva, A.N. Nyabera, O.O. Owa, M. Baidya, H.C. Sung, P.S. Taunk, S. Abdollahi, S. Charles, R.A. Gonnella, N. Gadi, K.T. Duong, J.N. Fawver, C. Ran, T.O. Jalonen, and I.V.J. Murray, "Small Molecules and Alzheimer's Disease: Misfolding, Metabolism and Imaging", *Curr. Alzheimer Res.* **12**, 000 (2015).

[14]N. Amdursky, Y. Erez, and D. Huppert, "Molecular Rotors: What Lies Behind the High Sensitivity of the Thioflavin-T Fluorescent", *Acc. Chem. Res.* **45**(9), 1548–1557 (2012).

[15]E.E. Nesterov, J. Skoch, B.T. Hyman, W.E. Klunk, B.J. Bacskai, and T.M. Swager, "In Vivo Optical Imaging of Amyloid Aggregates in Brain: Design of Fluorescent Markers", *Angew. Chem. Int. Ed.* **44**, 5452–5456 (2005).

[16]M. Ono, H. Watanabe, H. Kimura, and H. Saji, "BODIPY-Based Molecular Probe for Imaging of Cerebral Beta-Amyloid Plaques", *ACS Chem. Neurosci.* **3**, 319–324 (2012).

[17] H. Fu, M. Cui, P. Tu, Z. Pan, and B. Liu, "Evaluation of Molecules Based on the Electron Donor-Acceptor Architecture as Near-Infrared Beta-Amyloidal-Targeting Probes", *Chem. Commun.* **50**, 11875–11878 (2014).

[18] H. Fu, M. Cui, L. Zhao, P. Tu, K. Zhou, J. Dai, and B. Liu, "Highly Sensitive Near-Infrared Fluorophores for in Vivo Detection of Amyloid-beta Plaques in Alzheimer's Disease", *J. Med. Chem.* **58**, 6972–6983 (2015).

[19] C. Ran, X. Xu, S.B. Raymond, B.J. Ferrara, K. Neal, J. Brian, Z. Medarova, and A. Moore, "Design, Synthesis, and Testing of Difluoroboron Derivatized Curcumins as Near Infrared Probes for in vivo Detection of Amyloid-beta Deposits", *J. Am. Chem. Soc.* **131**, 15257–15261 (2009).

[20] X. Zhang, Y. Tian, Z. Li, X. Tian, H. Sun, H. Liu, A. Moore, and C. Ran, "Design and Synthesis of Curcumin Analogues for in vivo Fluorescence Imaging and Inhibiting Copper-Induced Cross-Linking of Amyloid beta Species in Alzheimer's Disease", *J. Am. Chem. Soc.* **135**, 16397–16409 (2013).

[21] X. Zhang, Y. Tian, C. Zhang, X. Tian, A.W. Ross, R.D. Moir, H. Sun, R.E. Tanzi, A. Moore, and C. Ran, "Near-Infrared Fluorescence Molecular Imaging of Amyloid beta Species and Monitoring Therapy in Animal Models of Alzheimer's Disease", *Proc. Nat. Acad. Sci. USA* **112**, 9734–9739 (2015).

[22] J. Yang, J. Yang, S.H. Liang, Y. Xu, A. Moore, and C. Ran, "Imaging Hydrogen Peroxide in Alzheimer's Disease via Cascade Signal Amplification", *Sci. Rep.* **6**, 35613 (2016).

[23] M. Martínez-Cifuentes, B. Weiss-López, and R. Araya-Maturana, "A Computational Study of Structure and Reactivity of N-Substitued-4-Piperidones Curcumin Analogues and their Radical Anions", *Molecules* **21**, 1658 (2016).

[24] E. Ferrari, R. Benassi, M. Saladini, G. Orteca, Z. Gazova, and K. Siposova, "In vitro Study on Potential Pharmacological Activity of Curcumin Analogues and Their Copper Complexes", *Chem. Biol. Drug Des.* **89**, 411–419 (2017).

[25] G. Xu, D. Wei, J. Wang, B. Jiang, M. Wang, X. Xue, S. Zhou, B. Wu, and M. Jiang, "Dyes and Pigments Crystal structure, optical properties and biological imaging of two curcumin derivatives", *Dye. Pigment.* **101**, 312–317 (2014).

[26] R. Sabate, L. Rodriguez-santiago, M. Sodupe, S.J. Saupe, and S. Ventura, "Thioflavin-T Excimer Formation Upon Interaction with Amyloid Fibers", *Chem. Commun.* **49**, 5745–5747 (2013).

[27]F. Peccati, J. Hernando, L. Blancafort, X. Solans-Monfort, and M. Sodupe, "Disaggregation-Induced Fluorescence Enhancement of NIAD-4 for the Optical Imaging of Amyloid-Beta Fibrils", *Phys. Chem. Chem. Phys.* **17**(30), 19718–19725 (2015).

[28]F. Peccati, M. Widniewska, X. Solans-Monfort, and M. Sodupe, "Computational Study on Donor-Acceptor Optical Markers for Alzheimer's disease: A Game of Charge Transfer and Electron Delocalization", *Phys. Chem. Chem. Phys.* **18**, 11634–11643 (2016).

[29]N.A. Murugan, R. Zalesny, J. Kongsted, A. Nordberg, and H. Ågren, "Promising Two-Photon Probes for In vivo Detection of Beta Amyloid Deposits", *Chem. Commun.* **50**, 11694–11697 (2014).

[30]G. Canard, M. Ponce-Vargas, D. Jacquemin, B. Le Guennic, A. Felouat, M. Rivoal, E. Zaborova, A. D'Aléo, and F. Fages, "Influence of the Electron Donor Groups on the Optical and Electrochemical Properties of Borondifluoride Complexes of Curcuminoid Derivatives: A Joint Theoretical and Experimental Study", *RSC Adv.* **7**, 10132–10142 (2017).

[31]X. Zhang, Y. Tian, P. Yuan, Y. Li, M.A. Yaseen, J. Grutzendler, A. Moore, and C. Ran, "A Bifunctional Curcumin Analogue for Two-Photon Imaging and Inhibiting Crosslinking of Amyloid Beta in Alzherimer's Disease", *Chem. Commun.* **50**, 11550–11553 (2014).

[32]R.G. Parr and W. Yang, *Density-Functional Theory of Atoms and Molecules*, Oxford University Press New York (1989).

[33]A.D. Becke, "Perspective: Fifty years of density-functional theory in chemical physics.", *J. Chem. Phys.* **140**(18), 18A301 (2014).

[34]K. Burke, J. Werschnik, and E.K.U. Gross, "Time-Dependent Density Functional Theory: Past, Present, and Future.", *J. Chem. Phys.* **123**, 062206 (2005).

[35]M.E. Casida and M. Huix-Rotllant, "Progress in Time-Dependent Density-Functional Theory.", *Ann. Rev. Phys. Chem.* **63**, 287–323 (2012).

[36]Y. Shao, Z. Gan, E. Epifanovsky, A.T. Gilbert, M. Wormit, J. Kussmann, A.W. Lange, A. Behn, J. Deng, X. Feng, D. Ghosh, M. Goldey, P.R. Horn, L.D. Jacobson, I. Kaliman, R.Z. Khaliullin, T. Kuś, A. Landau, J. Liu, E.I. Proynov, Y.M. Rhee, R.M. Richard, M.A. Rohrdanz, R.P. Steele, E.J. Sundstrom, H.L. Woodcock, P.M. Zimmerman, D. Zuev, B. Albrecht, E. Alguire, B. Austin, G.J.O. Beran, Y.A. Bernard, E. Berquist, K. Brandhorst, K.B. Bravaya, S.T. Brown, D. Casanova, C.M. Chang, Y. Chen, S.H. Chien, K.D. Closser, D.L. Crittenden, M. Diedenhofen, R.a. DiStasio, H. Do, A.D. Dutoi, R.G. Edgar, S. Fatehi,

L. Fusti-Molnar, A. Ghysels, A. Golubeva-Zadorozhnaya, J. Gomes, M.W. Hanson-Heine, P.H. Harbach, A.W. Hauser, E.G. Hohenstein, Z.C. Holden, T.C. Jagau, H. Ji, B. Kaduk, K. Khistyaev, J. Kim, J. Kim, R.A. King, P. Klunzinger, D. Kosenkov, T. Kowalczyk, C.M. Krauter, K.U. Lao, A. Laurent, K.V. Lawler, S.V. Levchenko, C.Y. Lin, F. Liu, E. Livshits, R.C. Lochan, A. Luenser, P. Manohar, S.F. Manzer, S.P. Mao, N. Mardirossian, A.V. Marenich, S.A. Maurer, N.J. Mayhall, E. Neuscamman, C.M. Oana, R. Olivares-Amaya, D.P. O'Neill, J.A. Parkhill, T.M. Perrine, R. Peverati, A. Prociuk, D.R. Rehn, E. Rosta, N.J. Russ, S.M. Sharada, S. Sharma, D.W. Small, A. Sodt, T. Stein, D. Stück, Y.C. Su, A.J. Thom, T. Tsuchimochi, V. Vanovschi, L. Vogt, O. Vydrov, T. Wang, M.A. Watson, J. Wenzel, A. White, C.F. Williams, J. Yang, S. Yeganeh, S.R. Yost, Z.Q. You, I.Y. Zhang, X. Zhang, Y. Zhao, B.R. Brooks, G.K. Chan, D.M. Chipman, C.J. Cramer, W.A. Goddard, M.S. Gordon, W.J. Hehre, A. Klamt, H.F. Schaefer, M.W. Schmidt, C.D. Sherrill, D.G. Truhlar, A. Warshel, X. Xu, A. Aspuru-Guzik, R. Baer, A.T. Bell, N.A. Besley, J.D. Chai, A. Dreuw, B.D. Dunietz, T.R. Furlani, S.R. Gwaltney, C.P. Hsu, Y. Jung, J. Kong, D.S. Lambrecht, W. Liang, C. Ochsenfeld, V.A. Rassolov, L.V. Slipchenko, J.E. Subotnik, T. Van Voorhis, J.M. Herbert, A.I. Krylov, P.M. Gill, and M. Head-Gordon, "Advances in Molecular Quantum Chemistry Contained in the Q-Chem 4 Program Package", *Mol. Phys.* **113**, 184–215 (2015).

[37] A.D. Becke, "Density-Functional Exchange-Energy Approximation with Correct Asymptotic Behavior", *Phys. Rev. A* **38**, 3098–3100 (1988).

[38] A.D. Becke, "A New Mixing of Hartree-Fock and Local Density Functional Theories", *J. Chem. Phys.* **98**, 1372 (1993).

[39] C. Lee, W. Yang, and R.G. Parr, "Development of the Colle-Salvetti Correlation-Energy Formula into a Functional of the Electron Density", *Phys. Rev. B* **37**, 785–789 (1988).

[40] C. Adamo and V. Barone, "Toward Reliable Density Functional Methods Without Adjustable Parameters: The PBE0 Model", *J. Chem. Phys.* **110**, 6158 (1999).

[41] Y. Zhao and D.G. Truhlar, "The M06 Suite of Density Functionals for Main Group Thermochemistry, Thermochemical Kinetics, Noncovalent Interactions, Excited States, and Transition Elements: Two New Functionals and Systematic Testing of Four M06-Class Functionals and 12 Other Functions", *Theor. Chem. Acc.* **120**, 215–241 (2007).

[42] J.D. Chai and M. Head-Gordon, "Systematic Optimization of Long-Range Corrected Hybrid Density Functionals.", *J. Chem. Phys.* **128**, 084106 (2008).

[43] M. Caricato, G.W. Trucks, M.J. Frisch, and K.B. Wiberg, "Electronic Transition Energies: A Study of the Performance of a Large Range of Single Reference Density Functional and Wave Function Methods on Valence and Rydberg States Compared to Experiment", *J. Chem. Theory Comput.* **6**, 370–383 (2010).

[44] S.S. Leang, F. Zahariev, and M.S. Gordon, "Benchmarking the Performance of Time-Dependent Density Functional Methods", *J. Chem. Phys.* **136**, 104101 (2012).

[45] M. Isegawa, R. Peverati, and D.G. Truhlar, "Performance of Recent and High-Performance Approximate Density Functionals for Time-Dependent Density Functional Theory Calculations of Valence and Rydberg Electronic Transition Energies.", *J. Chem. Phys.* **137**, 244104 (2012).

[46] A.D. Laurent and D. Jacquemin, "TD-DFT Benchmarks: A Review", *Int. J. Quantum Chem.* **113**(17), 2019–2039 (2013).

[47] A. Charaf-Eddin, A. Planchat, B. Mennucci, C. Adamo, and D. Jacquemin, "Choosing a Functional for Computing Absorption and Fluorescence Band Shapes with TD-DFT", *J. Chem. Theory Comput.* **9**, 2749 (2013).

[48] R. Krishnan, J.S. Binkley, R. Seeger, and J.A. Pople, "Self-Consistent Molecular Orbital Methods. XX. A Basis Set for Correlated Wave Functions", *J. Chem. Phys.* **72**, 650–654 (1980).

[49] P.M.W. Gill, B.G. Johnson, and J.A. Pople, "A Standard Grid for Density Functional Calculations", *Chem. Phys. Lett.* **209**, 506–512 (1993).

[50] A.D. Becke, "A Multicenter Numerical Integration Scheme for Polyatomic Molecules", *J. Chem. Phys.* **88**, 2547 (1988).

[51] J. Tomasi, B. Mennucci, and R. Cammi, "Quantum Mechanical Continuum Solvation Models", *Chem. Rev.* **105**, 2999–3093 (2005).

[52] T.N. Truong and E.V. Stefanovich, "A New Method for Incorporating Solvent Effect Into the Classical, ab initio Molecular Orbital and Density Functional Theory Frameworks for Arbitrary Shape Cavity", *Chem. Phys. Lett.* **240**, 253–260 (1995).

[53] V. Barone and M. Cossi, "Quantum Calculation of Molecular Energies and Energy Gradients in Solution by a Conductor Solvent Model", *J. Phys. Chem. A* **102**, 1995–2001 (1998).

[54] A.W. Lange and J.M. Herbert, "Polarizable Continuum Reaction-Field Solvation Models Affording Smooth Potential Energy Surfaces", *J. Phys. Chem. Lett.* **1**, 556–561 (2010).

[55] J. Tomasi, B. Mennucci, and E. Cancès, "The IEF Version of the PCM Solvation Method: An Overview of a New Method Addressed to Study Molecular Solutes at the QM ab initio Level", *J. Mol. Struct. THEOCHEM* **464**, 211–226 (1999).

[56] R. Cammi and B. Mennucci, "Linear Response Theory for the Polarizable Continuum Model", *J. Chem. Phys.* **110**, 9877–9886 (1999).

[57] M. Cossi and V. Barone, "Time-Dependent Density Functional Theory for Molecules in Liquid Solutions", *J. Chem. Phys.* **115**, 4708–4717 (2001).

[58] Z.Q. You, J.M. Mewes, A. Dreuw, and J.M. Herbert, "Comparison of the Marcus and Pekar Partitions in the Context of Non-Equilibrium, Polarizable-Continuum Solvation Models", *J. Chem. Phys.* **143**, 1–14 (2015).

[59] M. Segado, E. Benassi, and V. Barone, "A Twist on the Interpretation of the Multifluorescence Patterns of DASPMI", *J. Chem. Theory Comput.* **11**, 4803–4813 (2015).

[60] C. Hansch, A. Leo, and R.W. Taft, "A Survey of Hammett Substituent Constants and Resonance and Field Parameters", *Chem. Rev.* **91**, 165–195 (1991).

[61] S.P. Parimita, Y.V. Ramshankar, S. Suresh, and T.N. Guru Row, "Redetermination of Curcumin: (1E,4Z, 6E)-5-hydroxy-1,7-bis(4-hydroxy-3-methoxyphenyl)hepta-1,4,6-trien-3-one", *Acta Cryst.* **E63**, o860–o862 (2007).

[62] C.F. Chignell, P. Bilski, K.J. Reszka, A.G. Motten, R.H. Sik, and T.A. Dahl, "Spectral And Photochemical Properties of Curcumin", *Photochem. Photobiol.* **59**, 295–302 (1994).

[63] S.i. Kawano, Y. Inohana, Y. Hashi, and J.M. Lin, "Analysis of Keto-Enol Tautomers of Curcumin by Liquid Chromatography/Mass Spectrometry", *Chin. Chem. Lett.* **24**, 685–687 (2013).

[64] L. Shen and H.F. Ji, "Theoretical Study on Physicochemical Properties of Curcumin", *Spectrochim. Acta A* **67**, 619–623 (2007).

[65] S. Anjomshoa, M. Namazian, and M.R. Noorbala, "Is Curcumin a Good Scavenger of Reactive Oxygen Species? A Computational Investigation", *Theor. Chem. Acc.* **136**, 1–6 (2017).